



Fast and Automatic Identification of Contours for Girth Measurement on 3D Human Models with Variant Postures

Zhanqing Chen¹, Kai Tang² and Ajay Joneja³

¹Hong Kong University of Science and Technology, vitachen@ust.hk

²Hong Kong University of Science and Technology, mektang@ust.hk

³Hong Kong University of Science and Technology, joneja@ust.hk

ABSTRACT

We develop a novel method for fast and automatic identification of characteristic contours for measuring girths on digital 3D human models with various stable postures. For fast identification, the characteristic contours with salient topology and geometric features are selected among the multi-source geodesic iso-contours, which are constructed under a new Morse function as using multi-source points to compute geodesic distance instead of using solely one source point. The resulting iso-contours are stable in a wide range of postures due to the bending invariance of geodesic distance. Based on the characteristic contours, we develop an efficient algorithm to extract the contours for girth measurement. We present a number of experiments on 3D human body samples with variant postures to demonstrate the validity of our approach.

Keywords: iso-contour, girth measurement, posture.

DOI: 10.3722/cadaps.2013.321-337

1 INTRODUCTION

During the recent two decades 3-D scanning technology makes it possible to obtain digital data of a complete description of a human body. Working with the 3-D surface data has the advantage of being able to perform repeated measurements without the human subject being present. Therefore 3D body scanner has become notable for anthropometry. Within anthropometry measurement, body size and shape are the most important in ergonomic design and improvement of comfort in clothing. Anthropometry is the study of human body measurement and characterizes human body with linear distances between anatomical landmarks or circumferences at predefined locations. Its accuracy of traditional manual measurement is mainly affected by the expertise of the tailors.

Fruitful approaches to anthropometry measurements on 3D scanning data have been developed. However, these approaches have their respective disadvantages. In common, the measurement applies only to standard-posed models. Pargas et al. [18] constructed software to provide the user with tools to take measurements; the user must identify the landmarks manually by developing macros or short program. Much research effort has been applied to locating landmarks automatically. Geisen, et al. [8] presented an approach using image processing and neural networks. In order to obtain the traditional landmarks, subjects are marked with fiducials which are recorded by a color camera which images each three dimensional data point. This method, however, is limited to measuring only a subject's head; moreover it is only semi-automatic approach which needs fiducials pre-marking. The landmarks can be also be identified by analyzing the RGB information obtained from CCD cameras [22]. Nurre [17] located landmark fiducials based on physical geometry by finding the cusps on every slice of discrete points after the data are separated into six regions. Burnside's [5] utilized the Nurre's segmentation method and applied neural-network method to identify the 72 landmarks in the CAESAR (Civilian American and European Surface Anthropometry Resource) project.

There are other alternative approaches that attempt to locate landmarks automatically without prior marking [3][15], which usually depend on composing specific functions to locate the landmarks. Dekker [6] also investigated variant different operators in identifying salient landmarks. Leong et al [12] coupled image processing and computational geometry to extract features from a marker-less scanned body. Wang et al [21] employed fuzzy logic to recognize features in unorganized cloud points. Unfortunately, most of these methods are limited to locating only branch points. Template method is also explored by using predefined templates to identify landmarks on 3D models [2-4]. Ben et al [4] treated the landmarks' positions as random variables and formulated them as a Markov inference problem. Anguelov et al [2][3] used Markov network to embed an instance mesh into template. Their limitations are summarized in [15] and [11].

Landmark location and surface length are sensitive to posture during scanning, particularly in areas of high deformation. Xiao and Siebert [23] segmented body scan data into primary body parts in various postures based on geodesic distance. Geodesic distance is invariant under rigid transformation and isometric deformation. Inspired by their trial, we develop our algorithm to identify the characteristic contours with salient features based on the multi-source geodesic distance and the powerful Voronoi diagram technique. Comparing to the abovementioned method, and also validated by our experiments, we believe that our proposed method performs better in the body measurement. Our method is robust under large deformation since the body is separated by a group of Voronoi cells and the effect of deformation within its Voronoi cell acts only locally.

In this paper, the semantic definitions of body features are referred from ISO 8559. In the following sections, we introduce our approach in two parts: characteristic contours identification and the extraction of the contours for girth measurement.

2 CHARACTERISTIC CONTOURS IDENTIFICATION

Characteristic contours with topology and geometric features are chosen from the multisource geodesic iso-contours computed on a multisource geodesic distance field. Firstly, the multisource geodesic distance field is computed by presetting 5 source points which are the extreme points on the head, hands, and feet of a 3D human model. Secondly, iso-contours, Voronoi diagrams and the 1D tree skeleton are constructed by an interpolating manner method. The tree skeleton curve is obtained by connecting the barycenters of iso-contours according to the Reeb graph. Voronoi diagrams separate the body model into 5 major parts: arms, legs and torso-and-head segments, which provide the

topology of the human 3D model. Finally, the characteristic contours are identified through our defined topology and geometric features. An example is shown in Fig. 1.

In the following subsections, we first review the method of computing geodesic distance with multiple sources and introduce our novel method to construct the iso-contours and Voronoi diagrams on triangulated meshes. For details of skeleton extracting, references can be made from our previous work [14].

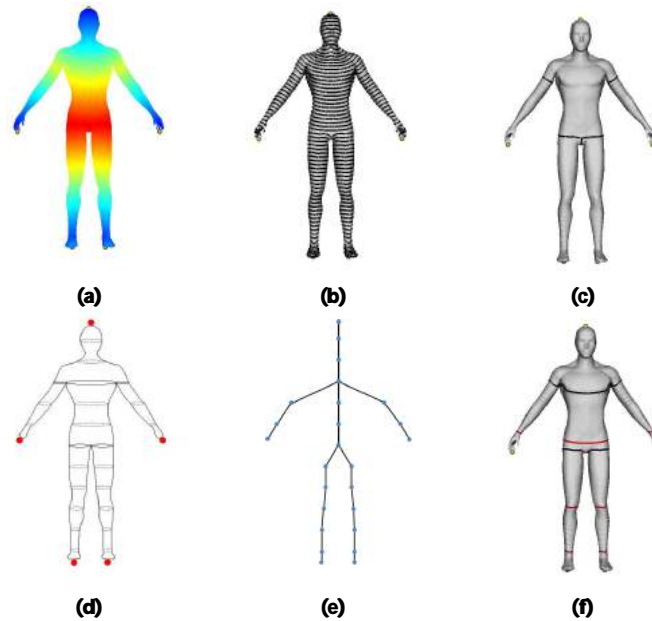


Fig. 1: (a) Geodesic distance field (b) Iso-contours (c) Voronoi diagrams (d) Critical iso-contours in Reeb Graph(Bold) (e) 1D Tree Skeleton (f) Characteristic contours.

2.1 Computing Multi-Source Geodesic Distance

Firstly we retrospect the implementation in [20] of the MMP algorithm [16] to establish the exact geodesic metric on a triangulated two-manifold surface M . The surface M studied in this paper comprises compact piecewise flat surfaces. The Hopf-Rinow theorem [9] and its adaption to general piecewise flat surfaces [1] ensure that a minimal geodesic exists between any two points. Denote the topology of a triangular mesh surface M by (V, E, F) , where V, E, F , are the vertex, edge and face sets, respectively.

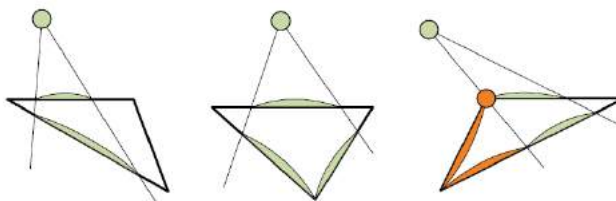
The MMP algorithm [16] establishes a distance function D_v on M such that for any point $p \in M$, denote $D_v(q)$ as the exact geodesic distance from q to v on M . The MMP algorithm partitions, the whole bunch of the faces in $F \in M$ into a 2D subdivision structure. To establish this structure, the following property is used. Inside every triangle in M , the geodesics must be straight lines. When crossing a triangle edge e , a geodesic must also be a straight line if the previous triangle is unfolded along e into the plane containing the next triangle (Fig. 2(b)). The vertices through which geodesics pass are named pseudo-sources. Singular vertices are defined for those whose total surrounding angle is larger than or equal to 2π .

From the triangles containing one or multiple sources p , a set of initial visibility wedges (VWs) are emitted. These VWs are propagated (Fig. 2(a)) until the whole bunch of the edges on the 2-manifold are covered. The different cases during the VW propagation are shown in Fig. 2(a). The pseudo-source of each VW can only be a singular vertex. To store the VW information in the local plane defined by each triangle, a 8-tuple $(b_0, b_1, d_0, d_1, \tau, \sigma, Id_{nv}, Id_{pt})$ is used in our approach (Fig.2(c)), denote b_0 and b_1 as parameters measuring the distance along the edge, the 2D unfolded position of the nearest pseudo-source s is encoded by its distances d_0 and d_1 to the endpoints b_0 and b_1 , respectively, Id_{nv} and Id_{pt} are the identifiers of s and the original point site p , respectively, τ indicates the side of edge on which s lies, and σ is the length of the geodesic path from $s = Id_{nv}$ back to the site $p = Id_{pt}$. While VW propagates, new wedges may intersect some existing wedges. Any two intersected wedge $(b_0^i, b_1^i, d_0^i, d_1^i, \sigma^i), i = 1, 2$ are updated by solving the equation below with unknown w (Fig. 2(d)):

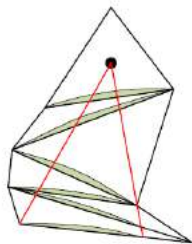
$$\sqrt{(w - s^1.x)^2 + (s^1.y)^2} + \sigma^1 = \sqrt{(w - s^2.x)^2 + (s^2.y)^2} + \sigma^2$$

Given one source point p^1 , the VW propagation builds a 2D subdivision structure (D_1, D_2, \dots, D_n) on M that satisfies $\bigcup_{i=1}^n D_i = \mathcal{M}$ and $D_i \cap D_j = \emptyset, i \neq j, i, j = 1, 2, \dots, n$. Each subdivision D_i has a corresponding $Id_{nv}(i)$ that is stored as a local 2D projection nv_i on each D_i . Given an arbitrary target position q on M , the geodesic path between p and q is computed as follows.

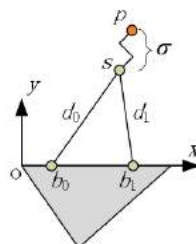
- 1) Find the subdivision cell D_q containing q . Set, $D_l = D_q, r = q$.
- 2) Connect r and the 2D position of nv_l by a line l , in the plane defined by D_l .
- 3) If $nv_l \neq p$, find the intersection x of the ray l with the boundary of D_l ; otherwise stop.
- 4) Find the adjacent subdivision D_j of D_l along the intersection x . Set $D_l = D_j, r = x$. Go back to (2).



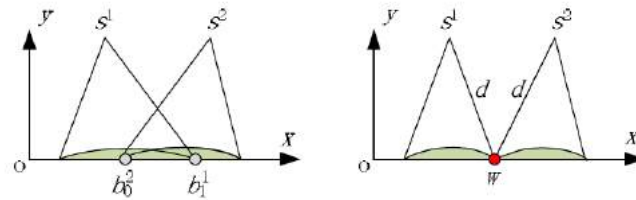
(a) Three cases in visibility wedge(VW) propagation



(b) VW in Flatten Triangle strips



(c) Encoding VW in a local plane



(d) Updating the intersecting VWs

Fig. 2: Geodesic paths encoding with visibility wedge propagation.

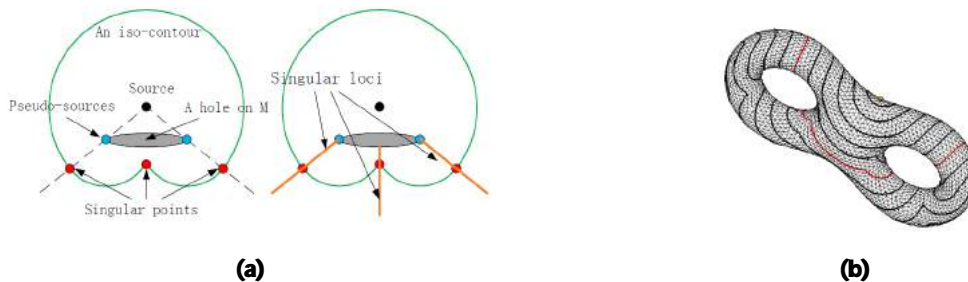


Fig. 3: (a) The existence of singular points in an iso-contour. For closed surfaces, the hole shown in the figure can be a polygonal obstacle such as a prism with sufficient height. (b) The iso-contours of a single source point on an eight model. The maximal geodesic distance on manifold is normalized to 1 and the iso-contour with value 0.5 is shown in red color which consists of three distinct closed curves connecting at the singular points.

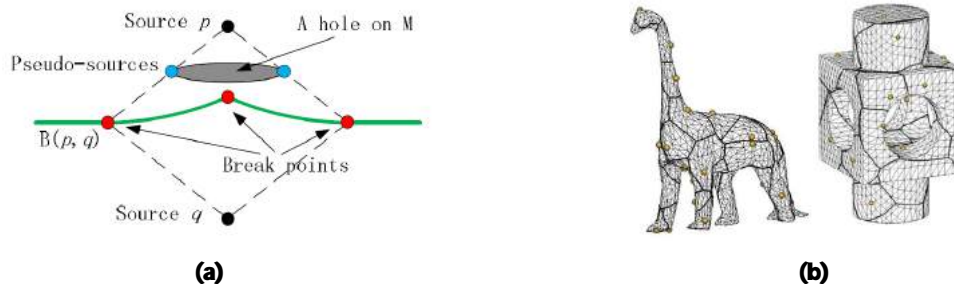


Fig. 4: (a) The existence of break points in a bisector. (b) Voronoi diagrams with random sampled source points on a genus 0 model and genus >0 model.

2.2 Computing Iso-contours and Voronoi Diagrams

An iso-contour of a site is defined as the trace of all the points whose distances to the site have a same specific value. The bisectors are traces of the points that are equidistant to the only two sites on the surface. All Voronoi cells are bounded mutually exclusive or semi-exclusive by bisectors, which construct the Voronoi diagrams as a result. The earlier simple interpolation methods for computing bisectors and iso-contours all assume that a bisector or iso-contour inside any triangular face is at

most one line segment. This causes serious errors when the mesh density is coarse. The correct iso-contour or bisector may require a turning point inside a triangular face.

Innovatively, we introduce the singular points on iso-contours which are defined as the locations where the nearest pseudo-source is changing from one to another. The schematic diagram (Fig. 3(a)) indicates that the prism with sufficient height affects the iso-contours in a 2D plane and the existence of singular points. The iso-contours at the singular points can have C_0 or C_1 continuity. An example of a genus-2 model with ten iso-contours is shown in Fig. 3(b). It clearly shows that the tangent discontinuities at the singular points and an iso-contour can be separated into three disjointed closed segments.

For computing the bisectors, the break points are defined by us as the locations at which the nearest pseudo-source is changing along the bisector from one side of a source point. Schematic diagram Fig. 4(a) shows the prism with sufficient height affecting the bisector in a 2D plane. A bisector consists of hyperbolic and line segments between breakpoints. The bisector is C_0 continuous at break points. Examples in Fig. 4(b) demonstrate the computed Voronoi diagrams on 3D models with different genus.

By introducing the singular points and break points, we can compute the complete iso-contours and bisectors. The remaining segments on the iso-contours except singular points and those on the bisectors (except breakpoints) are curves obtained by interpolation inside triangle faces.

2.3 Characteristic Contours Selection

Prior to our identification, merging and trimming of several nodes of the 1D skeleton are performed such as that multiple saddle nodes at the hands are merged together. The achieved neat and simple 1D tree skeleton serves for the procedures afterwards. The set \mathfrak{R} contains the whole bunch of the iso-contours only corresponding to the nodes in the obtained neat 1D skeleton.

Topologic characteristic contours are identified based on the Reeb graph. A point in a Reeb graph represents a level-set curve on a manifold defined by a function M . When M has no degenerate critical points on the manifold, it is a Morse function. In the past study, the height of the model and the geodesic distance from one source point are used as a Morse function. As a new Morse function, multi-source geodesic distance is computed for 3D body prototypes. The Reeb graph can be efficiently constructed by tracing the changes in the number of closed curves in each iso-contour (Fig. 1(b)). Moreover, the 1D tree skeleton could be also obtained (Fig. 1(e)). The critical points in the graph represent the critical level sets (illustrated by solid curves in Fig. 1(d)). When applied to human model, the critical points are meaningful. The saddle points naturally correspond to the armpits and the groin of the human body. Their corresponding contours estimate the elbow contours, chest contours, and thigh contours (black curves in Fig. 1(f)).

Geometric characteristic contours are defined based on the circumference. We denote the circumference for a contour $C_i \in \mathfrak{R}$ as a function $f(C_{id}, R_i, \theta_k)$. The R_i denotes the Voronoi cells. Voronoi diagram (Fig. 2(c)) divides the 3D body model into 5 Voronoi cells: arm (R_1 -left arm, R_2 -right arm), legs (R_3 -left leg, R_4 -right leg), and torso-and-head (R_5). Each iso-contour belongs to one unique Voronoi cell. For each iso-contour, the average geodesic distance $d_{avg}(C_{id})$ is calculated from all the points on the contour to its nearest source point. The whole bunch of iso-contours within every Voronoi cell is sorted by $d_{avg}(C_{id})$ in ascending order. We use θ to present the index of the ascending sequence such as $d_{avg}(\theta_1) < d_{avg}(\theta_2) \dots < d_{avg}(\theta_n)$.

Experientially, the contours in the arm region with the smallest circumferences enclose the wrist. In an identical manner, the iso-contours in the leg region with the smallest circumferences enclose the ankle as well.

$$C_{id}^* = \arg \min_{i=1,2,3,4} f(C_{id}, R_i, \theta_k)$$

Characteristic contours at the buttock are locally maximum enclosing curves. The buttock contours may be smaller than the chest contours. However the buttock characteristic contours are locally extreme inside the region near the boundary between the legs part and head-torso part.

$$C_d^* = \arg \max_{i=5} f(C_{id}, R_\varepsilon, \theta_k), R_U = R_3 \cap R_4 \cap R_5, \forall \varepsilon, |R_\varepsilon - R_U| < \varepsilon$$

The contours at the knees are locally minimum enclosing curves within the region which is the half length of the total leg length approximately. In our experiments we set $m = 2$.

$$C_{id}^* = \arg \min_{i=5} f(C_{id}, R_i, \theta_k), \forall m, |k - m| < \text{median}(\theta_j), j = 1, 2, \dots, n$$

3 EXTRACTION OF CONTOURS FOR GIRTH MEASUREMENT.

The characteristic contours are in general non-planar. Any contour for girth measure should be restricted to a 2D plane which mimics the measurement by an experienced tailor. It is preferable to obtain the intersection curves as contours for measurement between a 2D plane and the 3D model. The determination of the right 2D plane \mathbf{P} is through the process of projecting the characteristic contours by Principal Components Analysis (PCA) or robust PCA.

The widely used PCA is referred to as a dimensionality reduction algorithm. In our situation, the contours are 3 dimension data. The 2-dimensional space can be determined by the eigenvectors of the covariance matrix of data, which correspond to the larger two eigenvalues. The largest two eigenvalues are retained according to the practical assumption that anatomical lines are 2 dimensional. The eigenvectors corresponding to the two largest eigenvalues construct the projection plane. The eigenvector corresponding to the smallest eigenvalue represents the normal N_{PCA} orthogonal to the projection plane. In the classical PCA approach, the first component corresponds to the direction in which the projected observations have the largest variance. The second component is then orthogonal to the first and again maximizes the variance of the data. However, the projection plane (denoted by green color in Fig. 5) by using PCA deviates from the protuberance of the elbow characteristic contour (blue curve in Fig. 5) since PCA is sensitive to outliers (Fig. 5). The further utilization of robust PCA (ROBPCA) is a candidate solution. The ROBPCA method [10] combines ideas of projection pursuit (PP) [13] and robust covariance estimation. The PP part is used for the initial dimension reduction. Some ideal base on minimum covariance determinant (MCD) [19] estimator is applied. The normal N_{ROBPCA} based on using ROBPCA could be achieved. The projection plane by ROBPCA (red curve in Fig. 5) is more robust to outliers and coincides with the elbow characteristic contour tightly.

From the anthropometric view, the contours for measurement incline to be perpendicular to the skeleton, which is equivalent to prefer the smaller angle between the normal of the plane where the contour locates and the tangent of the skeleton. However the skeleton is discontinuous and does not have tangent at the skeleton node as it is constructed by connecting the skeleton nodes by line segments. As it is seen in Fig. 6, to avoid the discontinuity we interpolate a polynomial curve through the skeleton node itself and another two adjacent nodes. Denote T_{skel} the tangent of the polynomial curve segment. Denote θ_1, θ_2 the angle between the tangent T_{skel} and the normal N_{PCA} and N_{ROBPCA} respectively. Between the projection planes achieved by PCA and robust PCA, the one with a smaller

$\theta \in \{\theta_1, \theta_2\}$ is chosen. The resulting contour for measurement is the intersection curve between that projection plane and the triangulated model.

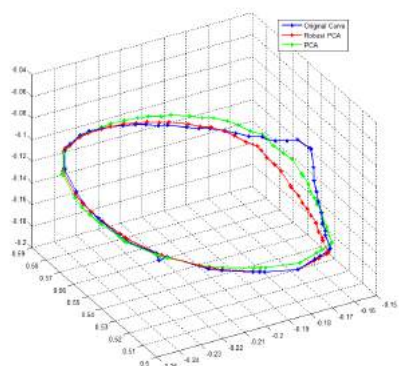


Fig. 5: Projected closed curves by PCA and ROBPCA.

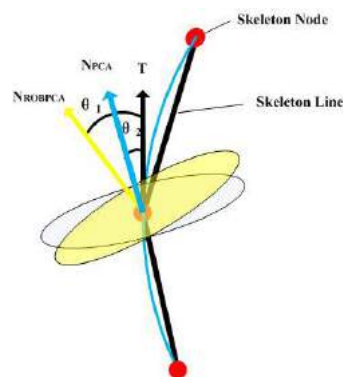


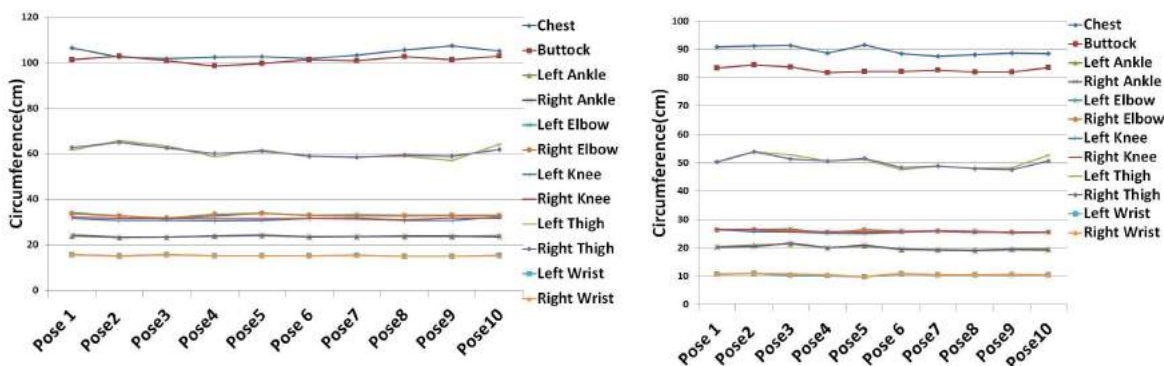
Fig. 6: The angles between the tangent of the skeleton curve and the normals of the projection planes.

4 EXPERIMENTS

We tested the proposed algorithms on triangulated surfaces of 3 different *Poser™* models in 10 different postures which are designed to simulate a real human body. Several methods are employed to check the consistence of the contours for measurement with variant postures quantitatively.

4.1 Circumference

Identifying the landmarks for the purpose of apparel design and manufacture is often utilized to finally calibrate. Therefore circumferences are extremely important features for clothing. We calibrated the circumferences of the contours for measurement. The experiment results indicate that the circumferences are consistent with different postures (Fig. 7). The circumferences standard deviation on the thigh and chest contours is larger than the standard deviation of contours on other body parts. The thigh circumferences, wrist circumferences, elbow circumferences, knee circumferences, and ankle circumferences have negligible differences between the right side and left side, coinciding well with the symmetry of human body.



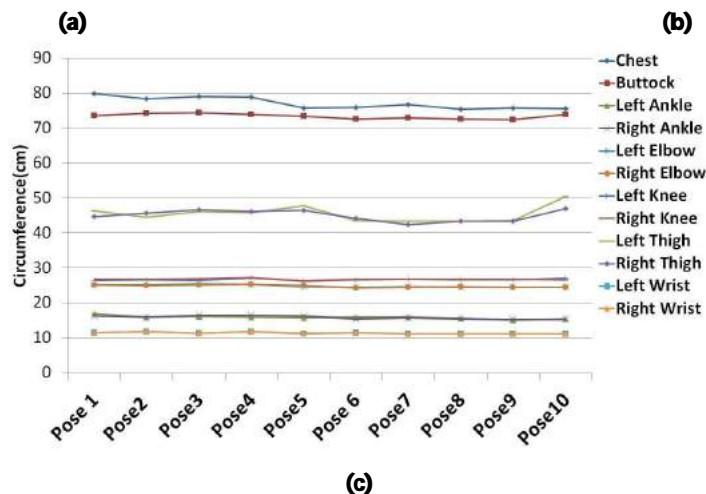


Fig. 7: (a) circumferences of male 3D models (b) circumferences of female 3D models (c) circumferences of child 3D models.

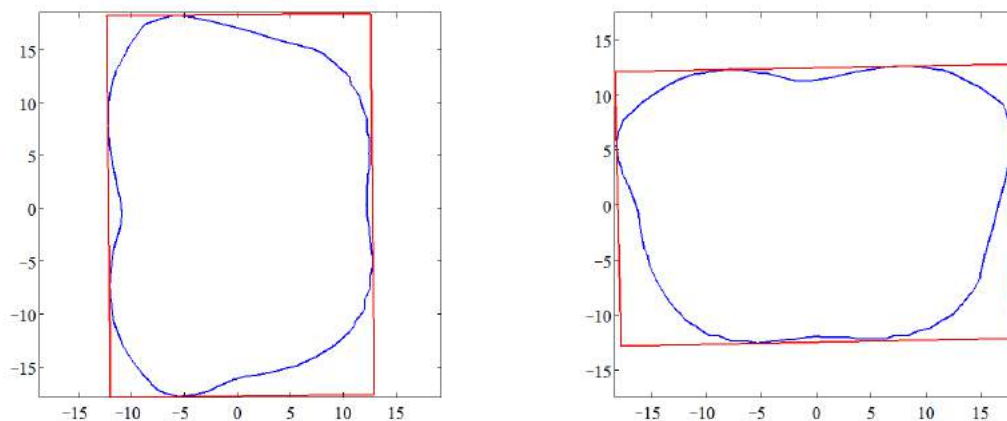


Fig. 8: Left is the bounding box on man's chest contours. Right is the contours after rotating the bounding box (the longer edge of the bounding box coincides with the X axis).

4.2 Polar Radius Consistency

We also explored the polar radius consistency on the contours with representable shapes like chest contours and buttock contours. The adjustment of the position and angle is needed to make individual contours for measurements with different postures coincide with each other maximally. We used the bounding box [7] to enclose the contours and then adjust the angle and position of the bounding box (Fig. 8). We also resample on the contours ranged from $[0, 2\pi]$ with 100 segments.

Fig. 9 shows the results of some hip contours. Fig. 10 shows the results of chest contours. The standard deviation of chest contours is lower than 0.6cm for all the tested 3D human body models. The standard deviation of buttock contours is smaller than 1.8cm for male and female 3D models (Fig. 9(b) and (d)). The standard deviation of buttock contours is beneath 0.4cm for child 3D models (Fig. 9(f)). The maximum standard deviation occurs when the contours' spike shifts which belongs to Pose

10 of man and woman 3D model. As demonstrated in the figure, the result ascribe to the one leg lifting posture is obviously different from other postures, which leads to the shape change of the buttock contours. The unit of polar plot is centimeter (cm).

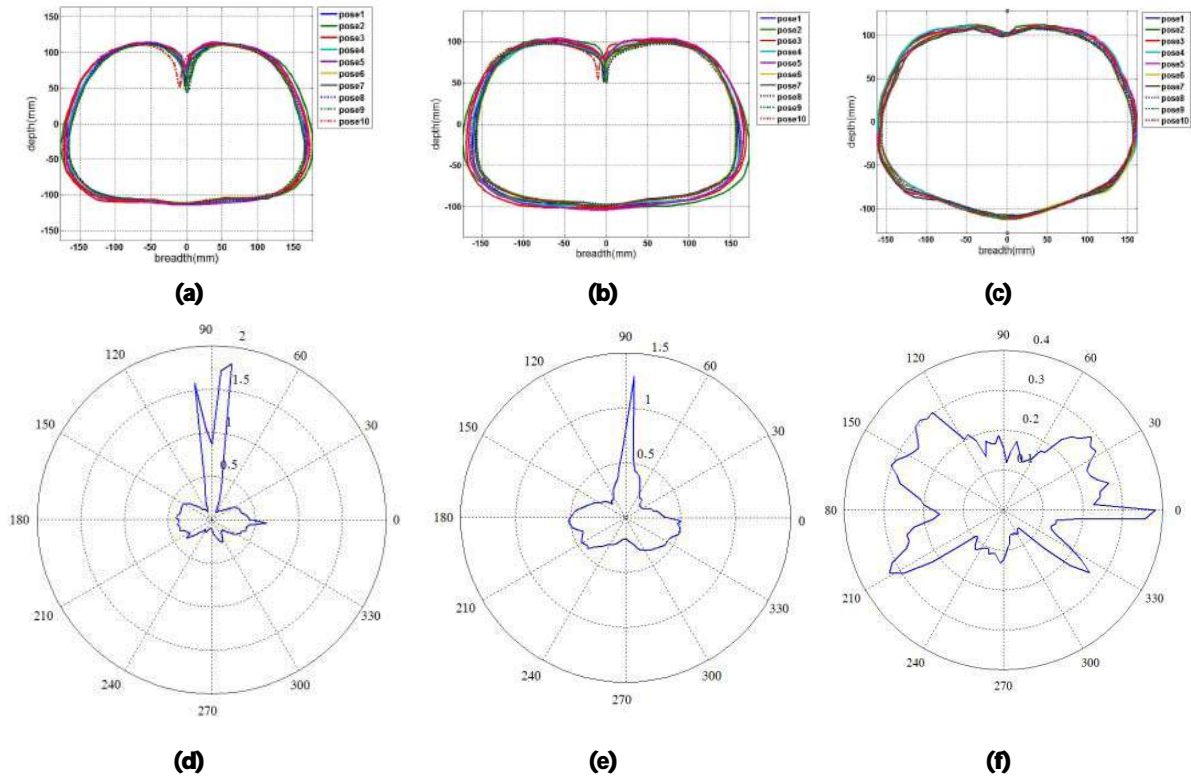
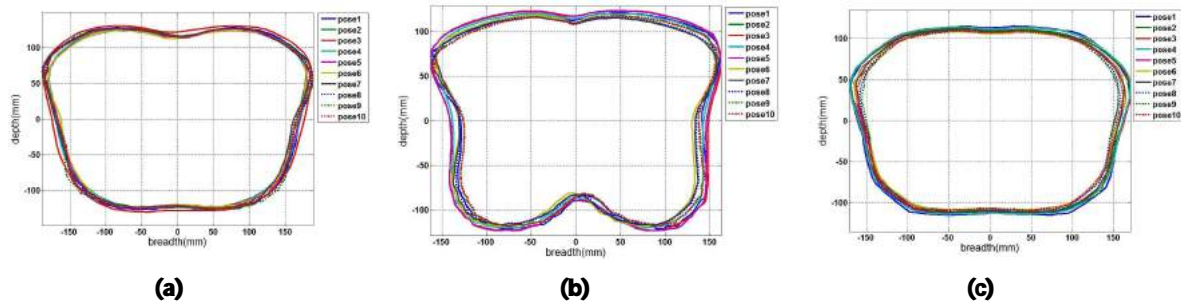


Fig. 9: (a) Plot of ten buttock contours on male 3D models. (b) Plot of ten buttock contours on female 3D models. (c) Plot of ten buttock contours on child 3D models. (d) Polar plot of buttock contours's standard deviation on male 3D models. (e) Polar plot of buttock contours's standard deviation on female 3D models. (f) Polar plot of buttock contours's standard deviation on child 3D models.



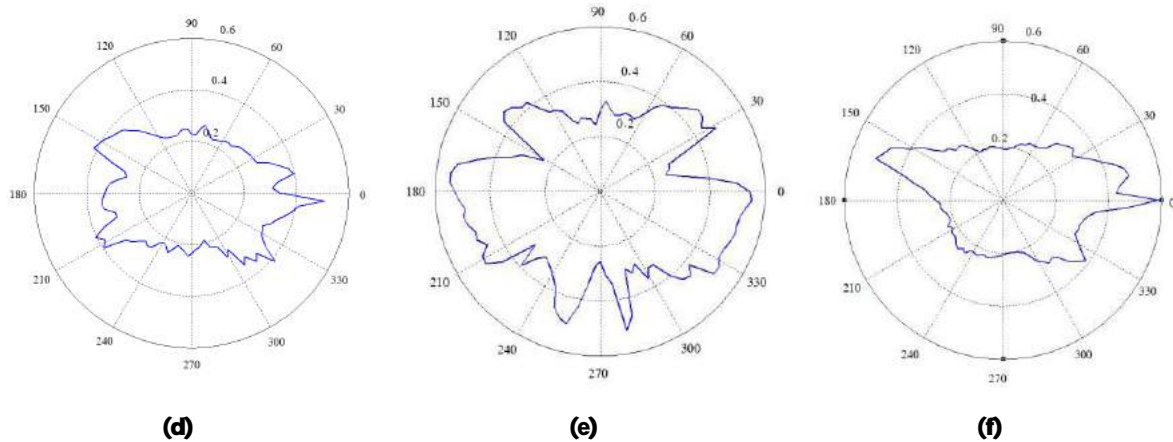


Fig. 10: (a) Plot of ten chest contours on male 3D models. (b) Plot of ten chest contours on female 3D models (c) Plot of ten chest contours on child 3D models. (d) Polar plot of chest contours standard deviation on male 3D models. (e) Polar plot of chest contours standard deviation on female 3D models. (f) Polar plot of chest contours standard deviation on child 3D models.

4.3 Hausdorff Distance

Hausdorff distance is the maximum minimum distance. It is defined as follows:

$$d_{\text{Hausdorff}}(A, B) = \max(\overrightarrow{d}(A, B), \overleftarrow{d}(B, A))$$

$$\overrightarrow{d}(A, B) = \max_{a \in A} (\min_{b \in B} d(a, b))$$

Hausdorff distance could be used to calibrate the integrity of the contours to match up with each other. We calculate the Hausdorff distance of resampled contours from one to the others. Box plots of the results are given in Fig. 11. The first column denotes the Hausdorff distances of hips which belong to male, female, and child (from top to down) models respectively. The second column depicts the Hausdorff distances of chest which belong to male, female and child (from top to down) models respectively. The first 5 postures of male, woman, child are squatting (Fig. 12-14). The last 5 postures are standing straight. As seen from the first column of the box plot (Fig 10), the box size of the last 5 postures is larger than that of the first 5 postures. The medians of the last 5 postures are larger than that of the first 5 postures. The test results validate that the influence of the variant postures on the targeted Hausdorff distance of chest is minimum.

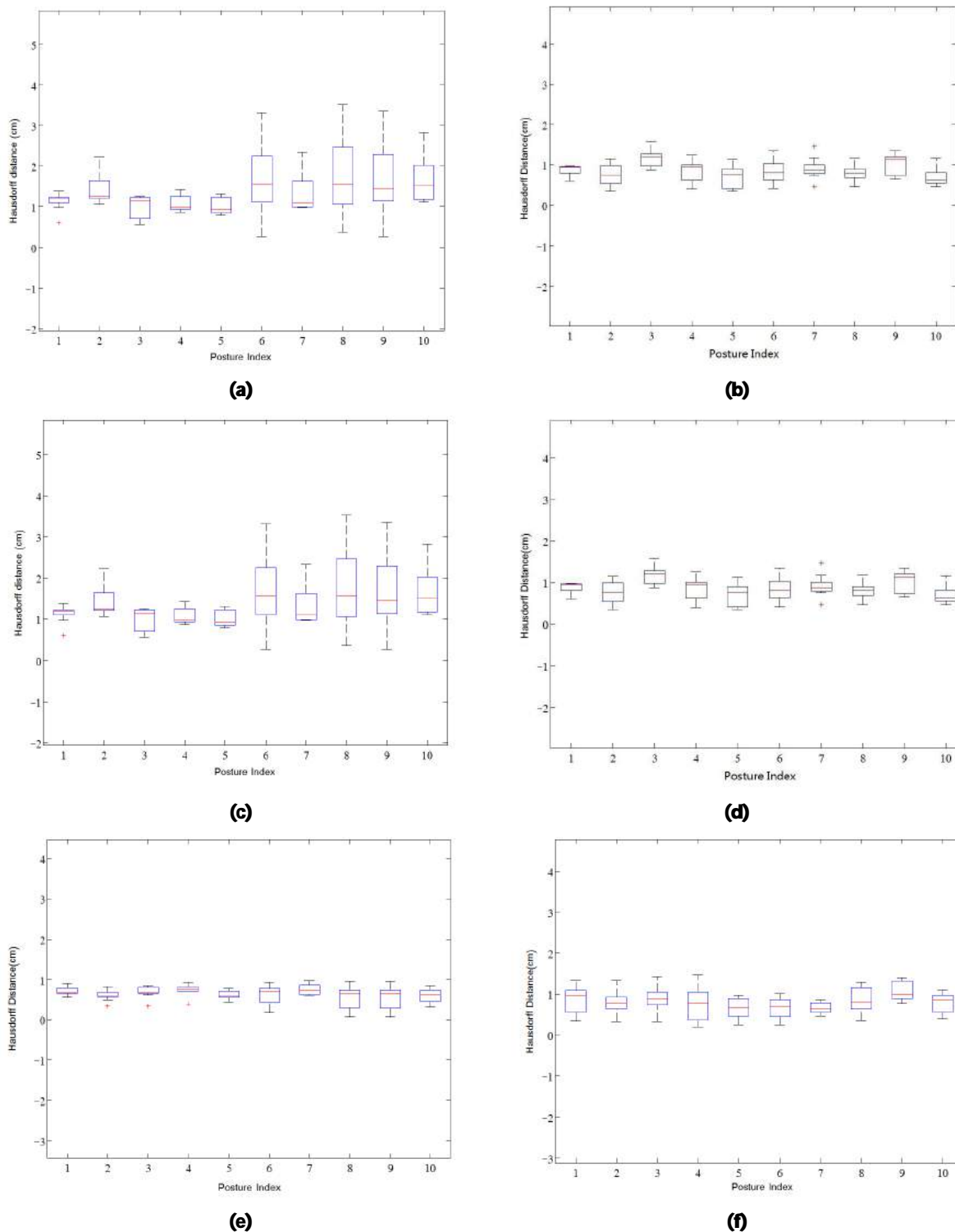


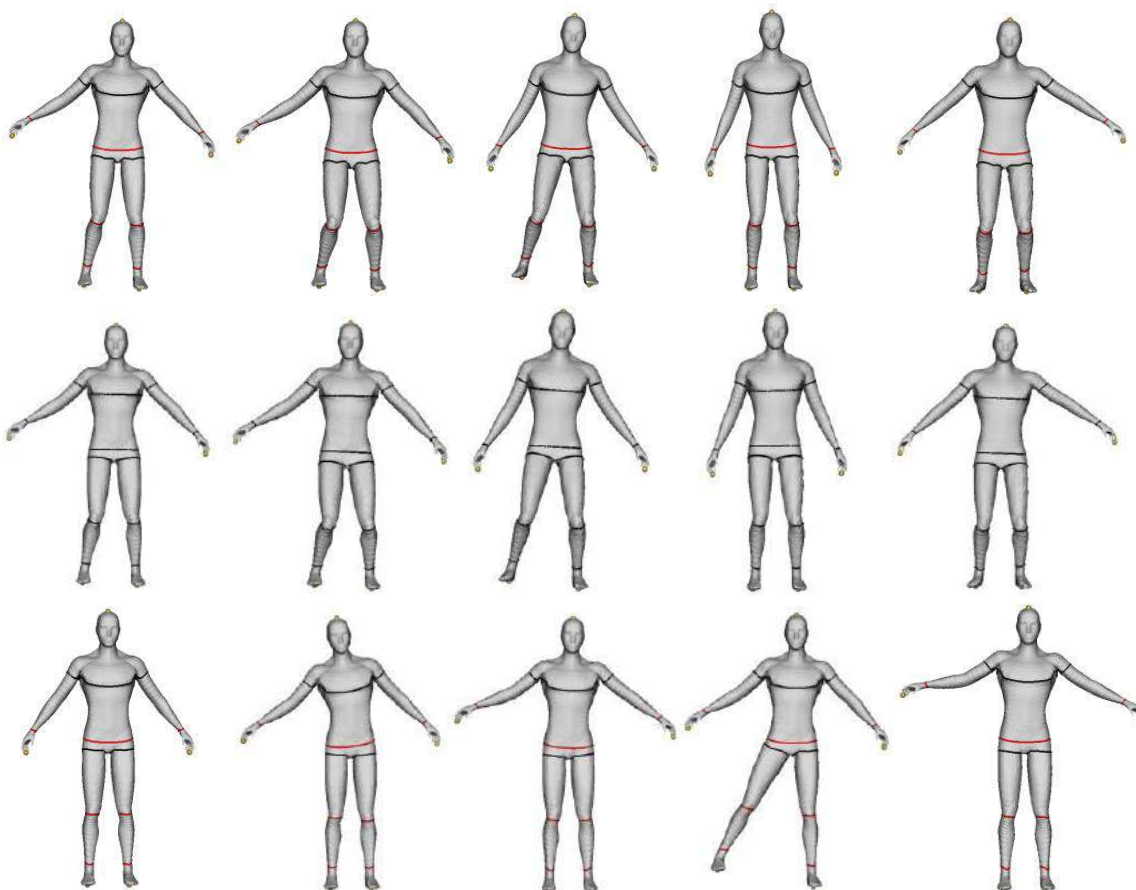
Fig. 11: (a) Hausdorff distance boxplot of male models **N**outtock (b) Hausdorff distance boxplot of male models **N**chesh (c) Hausdorff distance boxplot of female models **N**outtock (d) Hausdorff distance boxplot of female models **N**chesh (e) Hausdorff distance boxplot of female models **N**outtock (f) Hausdorff distance boxplot of female models **N**chesh
 Computer-Aided Design & Applications, 10(2), 2013, 321-337
 © 2013 CAD Solutions, LLC, <http://www.cadanda.com>

boxplot of female models chest (e) Hausdorff distance boxplot of child buttock (f) Hausdorff distance boxplot of child chest.

5 CONCLUSIONS

We have developed a novel method for estimating anthropometric parameters on various postures of a human 3D model. The method is based on the multi-source geodesic field. The Iso-contours and Voronoi diagram could be extracted from this field. Segmentation and Reeb graph could be achieved by Voronoi diagram. We used topologic feature and geometric feature locally on the segmented subregions to identify the characteristic iso-contours fast and automatically. Optimized PCA and Robust PCA are applied to the captured 3D characteristic iso-contours to achieve their planar counterparts for the measurement. In the experiments, we apply our methods to representative 3D human body models with different postures. We test the circumference, the standard deviation of polar radius, and the Hausdorff distance. The results demonstrate that the contours for measurement are consistent with each other.

In the future, the application of contours at other locations will be explored by our method. In addition, real human body scan data will be collected for correlation purpose and further research.



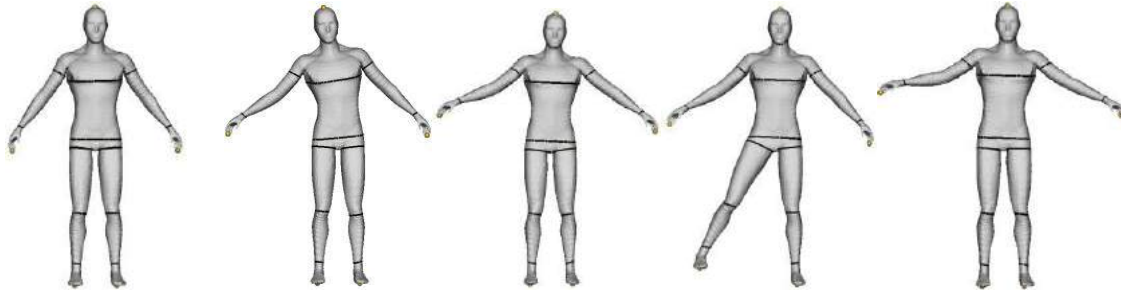
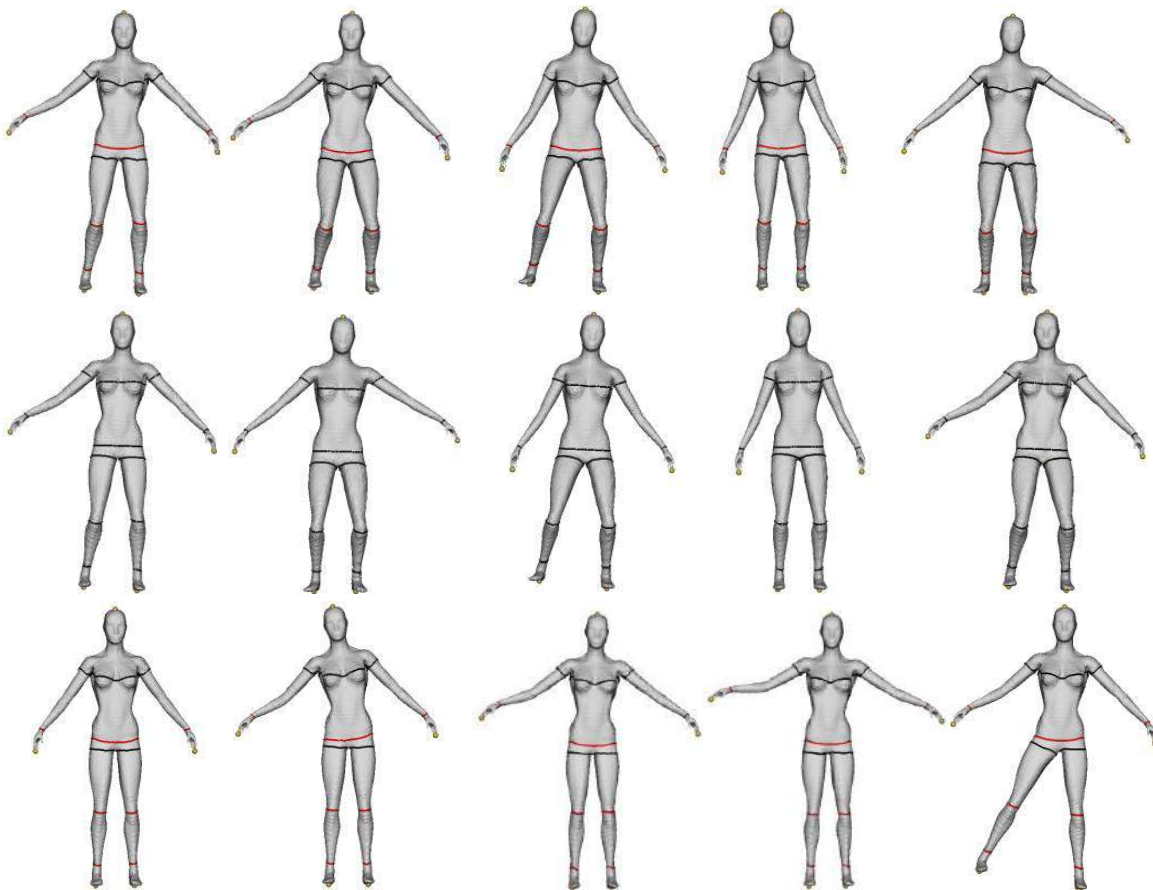


Fig. 12: First row and third row are the results of characteristic contours on 3D male models. Topologic characteristic contours are masked by black color. Geometric characteristic contours are colored by red. Second row and fourth row indicate the contours for measurement.



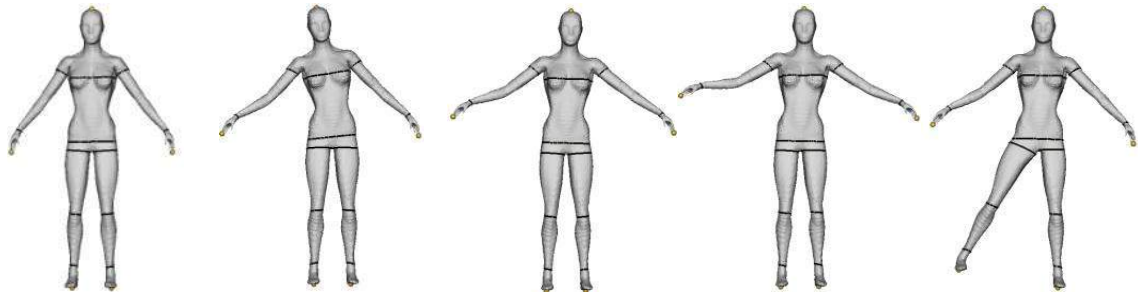
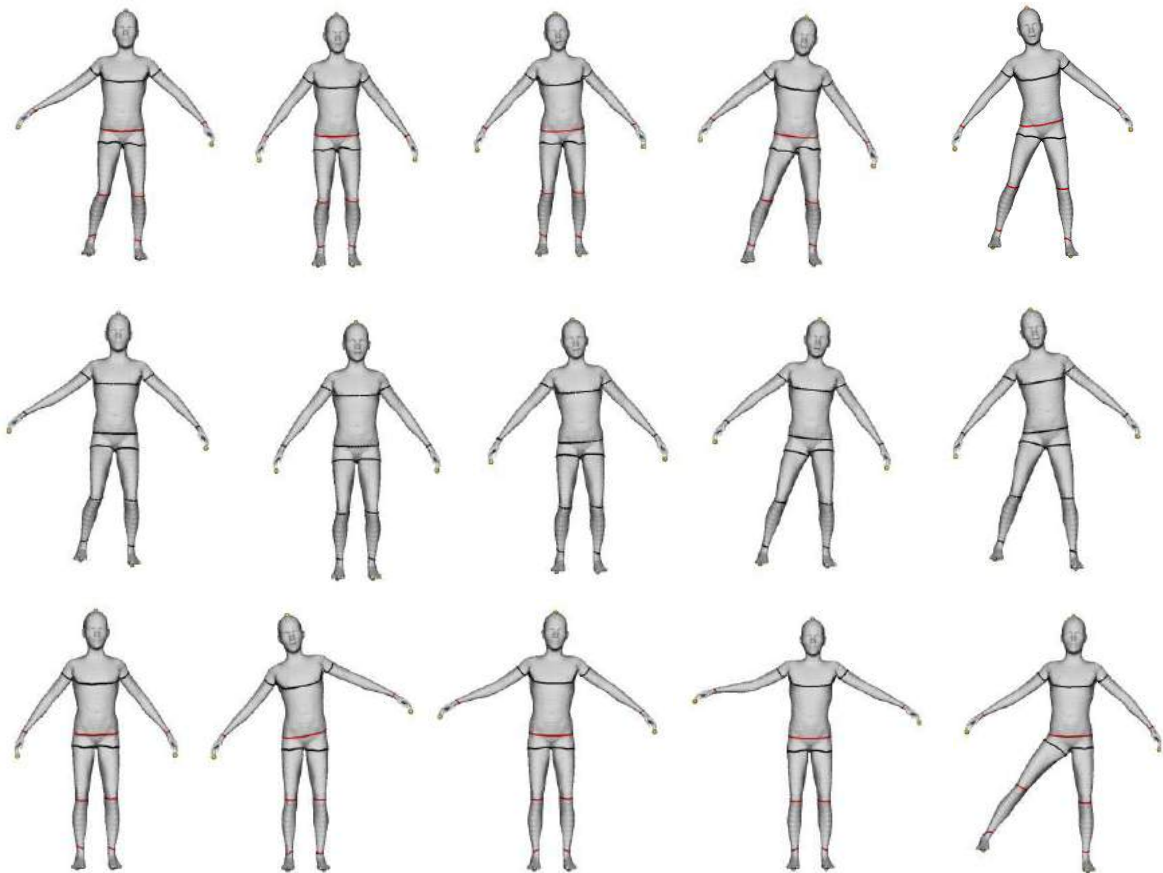


Fig. 13: First row and third row are the results of characteristic contours on 3D female models. Topologic characteristic contours are masked by black color. Geometric characteristic contours are colored by red. Second row and fourth row indicate the contours for measurement.



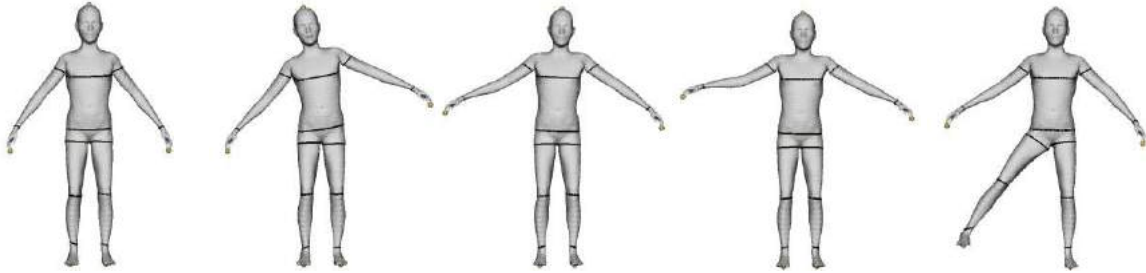


Fig. 14: First row and third row are the results of characteristic contours on 3D child models. Topologic characteristic contours are masked by black color. Geometric characteristic contours are colored by red. Second row and fourth row indicate the contours for measurement.

REFERENCES

- [1] Aleksandrov, A. D.; Zalgaller, V. A.: *Intrinsic Geometry of Surfaces*, AMS Publisher, 1967.
- [2] Anguelov, D.; Srinivasan, P.; Koller, D.; Thrun, S.; Pang, H.; Davis, J.: The correlated correspondence algorithm for unsupervised registration of nonrigid surfaces, In *Advances in Neural Information Processing Systems*, 17, 2005, 33-40.
- [3] Anguelov, D.; Srinivasan, P.; Koller, D.; Thrun, S.; Pang, H.; Davis, J.: Scape: shape completion and animation of people, *ACM Trans. Graph.*, 24(3), 2005, 408-416.
- [4] Azouz, Z. B.; Shu, C.; Mantel, A.: Automatic Locating of Anthropometric Landmarks on 3D Human Models, *Third International Symposium on 3D Data Processing, Visualization and Transmission*, 2006, 750-757.
- [5] Burnsides, D. B.; Boehmer, M.; Robinette, K. M.: 3-D landmark detection and identification in the CAESAR project, *Proceedings of the Third International Conference on 3-D Digital Imaging and Modeling Conference*, 2001, 393-398.
- [6] Dekker, L.; Douros, I.; Buxton, B. and Treleaven, P.: Building Symbolic Information for 3D Human Body Modeling from Range Data, In *Proceedings of the Second International Conference on 3-D Digital Imaging and Modeling (3DIM'99)*, 1999, 388-397.
- [7] Freeman, H.; Shapira, R.: Determining the minimum-area encasing rectangle for an arbitrary closed curve, *Communications of the ACM*, 18, 1975, 409-413.
- [8] Geisen, G.; Mason, G. P.; Houston, V.; Whitestone, J.; McQuiston, B.; Beattie, A.: Automatic Detection, Identification, and Registration of Anatomical Landmarks, *Proc. 39th Annual Meeting of the Human Factors and Ergonomics Society*, 2, 1995, 750-753.
- [9] Hopf, H.; Rinow, W.: Über den Begriff der vollständigen differentialgeometrischen Fläche, *Comment. Math. Helv.*, 3, 1931, 209-225.
- [10] Hubert, M.; Rousseeuw, P.J.; Van den Branden, K.: ROBPCA: a New Approach to Robust Principal Component Analysis, *Journal of Technometrics*, 47, 2005, 64-79.
- [11] Jones, P. R.; Rioux, M.: Three-dimensional surface anthropometry: Applications to the human body, *Optics and Lasers in Engineering*, 28, 1997, 89-117.
- [12] Leong, I. F.; Fang, J. J.; Tsai, M. J.: Automatic body feature extraction from a marker-less scanned human body, *Computer-Aided Design*, 39(7), 2007, 568-582.
- [13] Li, G.; Chen, Z.: Projection-Pursuit Approach to Robust Dispersion Matrices and Principal Components: Primary Theory and Monte Carlo, *Journal of the American Statistical Association*, 80, 1985, 759-766.

- [14] Liu, Y. J.; Chen, Z. Q.; Tang, K.: Construction of Iso-contours, Bisectors and Voronoi Diagrams on Triangulated Surfaces, *IEEE transactions on Pattern Recognition and Machine Intelligence*, 33, 2011, 1502-1517.
- [15] Lu, J. M.; Wang, M. J.: Automated anthropometric data collection using 3D whole body scanners, *Expert Systems with Applications*, 35, 2008, 407-414.
- [16] Mitchell, J.; Mount, D. M.; Papadimitriou, C.H.: The Discrete Geodesic Problem, *SIAM Journal of Computing*, 16(4), 1987, 647-668.
- [17] Nurre, J.: Locating Landmarks on Human Body Scan Data, *International Conference on Recent Advances in 3D Digital Imaging and Modeling*, 1997, 289-295.
- [18] Pargas, R.P.; Staples, N.J.; Davis, J.S.: Automatic measurement extraction for apparel from a three-dimensional body scan, *Optics and Lasers in Engineering*, 28, 1997, 157-172.
- [19] Rousseeuw, P.J.: Least Median of Squares Regression, *Journal of the American Statistical Association*, 79, 1984, 871-880.
- [20] Surazhsky, V.; Surazhsky, T.; Kirsanov, D.; Gortler, S.; Hoppe, H.: Fast Exact and Approximate Geodesics on Meshes, *Proc. ACM SIGGRAPH*, 2005, 553-560.
- [21] Wang, C.; Chang, T. and Yuen, M.: From Laser-Scanned Data to Feature Human Model: A System Based on Fuzzy Logic Concept, *Computer Aided Design*, 35, 2003, 241-253.
- [22] Wang, M. J.; Wu, W.Y.; Lin, K. C.; Yang, S. N., Lu, J. M.: Automated anthropometric data collection from three-dimensional digital human models, *International Journal of Advanced Manufacturing Technology*, 32, 2007, 109-115.
- [23] Xiao, Y.; Siebert, P.; Werghi, N.: A Discrete Reeb Graph Approach for the Segmentation of Human Body Scans, *Proc. Int'l Conf. 3D Digital Imaging and Modeling*, 2003, 378-385.